

**Supporting Information: Transport characterization of solid-state Li_2FeS_2
cathodes from a porous electrode theory perspective**

Tim Bernges*^[a], Lukas Ketter^[a,b], Bianca Helm^[c], Marvin A. Kraft^[d], Kimberly A.

See^[e], Wolfgang G. Zeier*^[a,b,d]

*^aInstitute of Inorganic and Analytical Chemistry, University of Münster, D-48149
Münster, Germany*

*^bInternational Graduate School for Battery Chemistry, Characterization, Analysis,
Recycling and Application (BACCARA), University of Münster, D-48149 Münster,
Germany*

*^cBavarian Center for Battery Technology (BayBatt), University of Bayreuth, D-
95447 Bayreuth, Germany*

*^dInstitute of Energy Materials and Devices (IMD), IMD-4: Helmholtz-Institut Münster,
Forschungszentrum Jülich, 48149 Münster, Germany*

*^eDivision of Chemistry and Chemical Engineering, California Institute of
Technology, Pasadena, 91125 California, USA*

Synthesis and structure of Li_2FeS_2 and $\text{Li}_{5.5}\text{PS}_{4.5}\text{Cl}_{1.5}$

The cathode-active material Li_2FeS_2 and solid electrolyte $\text{Li}_{5.5}\text{PS}_{4.5}\text{Cl}_{1.5}$ were synthesized by high-temperature solid-state synthesis and structurally characterized conducting X-ray diffraction experiments and subsequent Pawley fits and Rietveld refinements. For synthesis of Li_2FeS_2 , stoichiometric amounts of Li_2S (Thermo Scientific Chemicals, 99.9%) and FeS (Thermo Fischer, Alfa Aesar, 99.9%) were mixed in an agate mortar for 15 minutes, pelletized and placed in carbon-coated quartz ampoules. The ampoules were previously dried under dynamic vacuum for one hour at 1073 K. The synthesis was performed at 773 K (heating rate of 100 K per hour) with a dwelling time of five days (uncontrolled cooling rate).

The solid electrolyte $\text{Li}_{5.5}\text{PS}_{4.5}\text{Cl}_{1.5}$ was synthesized in a two step synthesis from the reactants Li_2S (Thermo Scientific Chemicals, 99.9%), P_2S_5 (Sigma Aldrich, 99%) and LiCl (Sigma Aldrich, 99%). The reactants were mixed in an agate mortar for 15 minutes, pelletized and placed in previously dried carbon-coated quartz ampoules. Two synthesis steps were performed at 723 K (heating rate 100 K per hour) for three days of dwelling time each (uncontrolled cooling rate), with intermediate grinding and repelletizing of the reactant mixture.

Quality control of the synthesized materials was conducted by X-ray diffraction and subsequent Pawley fits and Rietveld refinements to the diffractograms. X-ray diffractograms were measured on a Stoe STADI-P diffractometer using Mo-K α radiation ($\lambda = 0.70930 \text{ \AA}$) in Debye-Scherrer geometry. Data were collected in a 2θ range 4 to 55° with a step size of 0.015° and a scan speed of 60.0 s/step. Pawley fits were conducted by subsequently fitting the background using a Chebyshev polynomial, the peak shape using a Thompson-Cox-Hastings modified pseudo-Voigt

function, a zero offset and the lattice parameters. For the Rietveld refinements, the atomic positions and thermal displacement parameters were subsequently refined.

The majority of the reflections in the diffractogram (Figure S1 a) of Li_2FeS_2 can be assigned to the expected phase with space group $P\bar{3}m1$ and the obtained lattice parameters $a = b = 3.9135 \text{ \AA}$ and $c = 6.3019 \text{ \AA}$ agree with literature reports, confirming the successful synthesis. The structure of Li_2FeS_2 in its pristine state is constructed from alternating layers of face-sharing $\text{Li}^+\text{-S}^{2-}$ octahedra and $(\text{Li}^+, \text{Fe}^{2+})\text{-S}^{2-}$ tetrahedra, where Li^+ and Fe^{2+} share the tetrahedral position (Figure S1 b). Additional reflections, not described by the Li_2FeS_2 phase, are observed and can be assigned to impurities of elemental Fe and Li_2S . We acknowledge the low likelihood of forming elemental Fe as impurity phase. Nonetheless, it was the best match to the reflection around $q = 3 \text{ \AA}$ of our phase search of phases consisting of the elements: S, Fe, Li, O, Si. Rietveld refinements suggest that the total amount of impurities can be estimated to lie below <5 wt.% so that no severe influence on the overall performance of Li_2FeS_2 is expected.

To circumvent influences of varying impurity phase degrees on the conclusions of this study, all experiments were conducted using the same synthesis batch of Li_2FeS_2 .

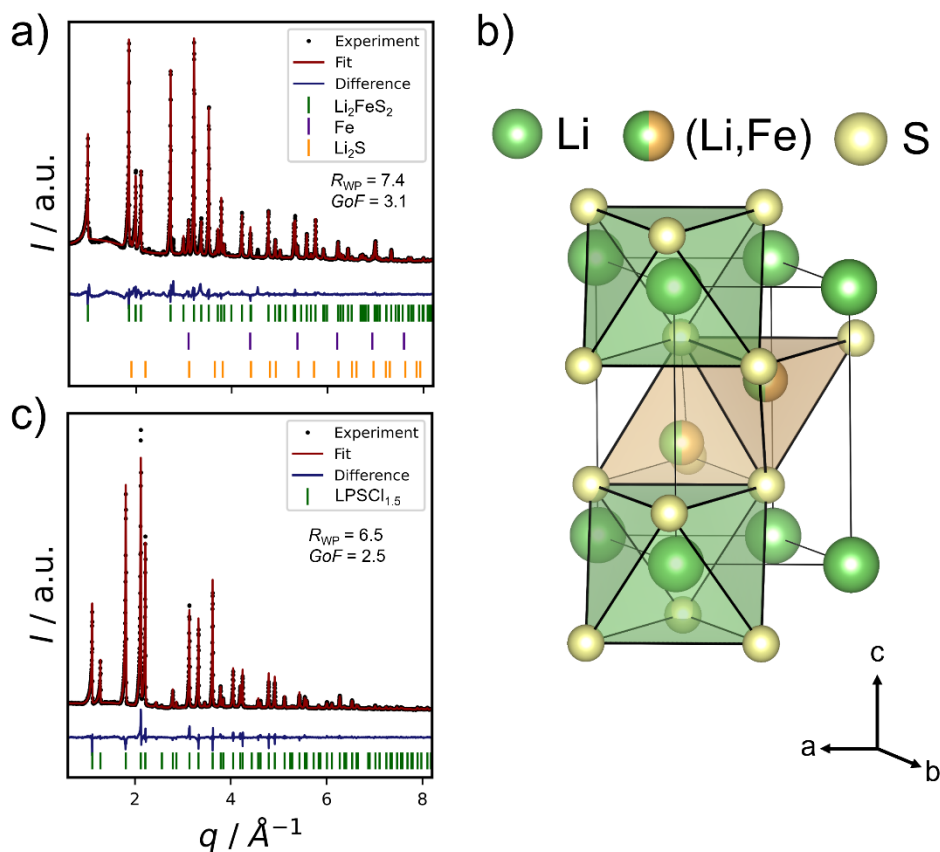


Figure S1. a) X-ray diffraction pattern of as-synthesized Li_2FeS_2 and corresponding Rietveld refinements. The majority of the reflections can be assigned to Li_2FeS_2 in space group $P\bar{3}m1$, with additional reflections corresponding to low amounts of Li_2S and elemental Fe b) Unit cell of Li_2FeS_2 in space group $P\bar{3}m1$ built up by layers of Li-S octahedra (green polyhedral), and (Li,Fe)-S tetrahedral (orange polyhedral), where Li and Fe share the crystallographic position in equal parts. c) Diffraction pattern of $\text{Li}_{5.5}\text{PS}_{4.5}\text{Cl}_{1.5}$ and corresponding Rietveld refinements.

The corresponding diffraction pattern collected for $\text{Li}_{5.5}\text{PS}_{4.5}\text{Cl}_{1.5}$ (LPSC1.5) is well-described by the expected phase in space group $F\bar{4}3m$ (Figure S1 c). Furthermore,

the refined lattice parameters of $a = b = c = 9.8108(2)$ corroborated the success of the synthesis. For details of the structure the reader is referred to literature.¹

Table S1. Structural parameters obtained from Rietveld refinements against Mo-K α X-ray diffraction data of Li₂FeS₂.

Li ₂ FeS ₂ structure from Mo K α 1-diffraction (space group $P\bar{3}m1$); $a = b = 3.9120(2)$ Å, $c = 6.2995(4)$ Å Additional phases: Li ₂ S – 1.1 wt.%; Fe – 2.1 wt.%; GoF = 3.1, $R_{wp} = 7.2\%$					
Atom	x/a	y/b	z/c	Occ.	$B_{eq}/\text{Å}^2$
S1	1/3	2/3	0.250(7)	1	1.1(1)
Fe1	1/3	2/3	0.631(6)	0.5	1.1(1)
Li1	1/3	2/3	0.631(6)	0.5	1.1(1)
Li2	0	0	0	1	3

Table S2. Structural parameters obtained from Rietveld refinements against Mo-K α X-ray diffraction data of Li_{5.5}PS_{4.5}Cl_{1.5}.

Li _{5.5} PS _{4.5} Cl _{1.5} structure from Mo K α 1-diffraction (space group $F\bar{4}3m$); $a = b = c = 9.8108(5)$ Å Additional phases: LiCl – 1.5 wt.%; GoF = 2.5, $R_{wp} = 6.5\%$					
Atom	x/a	y/b	z/c	Occ.	B _{eq} /Å ²
S1	0.25	0.25	0.75	0.14	2.4(2)
Cl1	0.25	0.25	0.75	0.86	2.4(2)
S2	0	0	1	0.45	3.0(2)
Cl2	0	0	1	0.55	3.0(2)
S3	0.1207(4)	-0.1207(4)	0.6207(4)	1	4.0(1)
P1	0	0	0.5	1	2.1(2)
Li1	0.261	0.048	0.548	0.148	5.1
Li2	0.328	0.031	0.621	0.318	5.1

General information about the prepared cathodes

Table S3. Information about the prepared cathodes with varying CAM volume fraction ϕ_{CAM} . A conversion of the tested rates of 0.134 C to terms of current densities in units of $\text{mA}\cdot\text{cm}^{-2}$ considering a theoretical capacity of $300 \text{ mAh}\cdot\text{g}^{-1}$ and a cathode mass of 12 mg, 18 mg* and 24 mg**. The cathode thicknesses are approximated by 85% of the theoretical density of the composite and the cathode mass. Current densities are back-calculated to C-rate by considering the theoretical specific capacity of $300 \text{ mAh}\cdot\text{g}^{-1}$.

	C-rate →		$i \rightarrow$	$i \rightarrow$	$i \rightarrow$	$i \rightarrow$
	i		C-rate	C-rate	C-rate	C-rate
ϕ_{CAM}	0.134 C /	$L /$	0.6	1.3	2.5	5.1
	$\text{mA}\cdot\text{cm}^{-2}$	μm	$\text{mA}\cdot\text{cm}^{-2}$	$\text{mA}\cdot\text{cm}^{-2}$	$\text{mA}\cdot\text{cm}^{-2}$	$\text{mA}\cdot\text{cm}^{-2}$
			$/ \text{h}^{-1}$	$/ \text{h}^{-1}$	$/ \text{h}^{-1}$	$/ \text{h}^{-1}$
0.32	0.24	85	0.33	0.71	1.37	2.80
0.41	0.31	82	0.26	0.57	1.10	2.24
0.51	0.37	79	0.22	0.48	0.91	1.86
0.62	0.43	76	0.19	0.41	0.78	1.60
0.74	0.49	73	0.16	0.36	0.69	1.40
0.74*	0.73	110	0.11	0.24	0.46	0.93
0.74**	0.98	145	0.08	0.18	0.34	0.70
1	0.61	67	0.13	0.29	0.55	1.12

Experimental characterization of the partial conductivities

Chronoamperometry in electron- and ion-blocking conditions

The electronic and ionic conductivity of all $\text{Li}_{5.5}\text{PS}_{4.5}\text{Cl}_{1.5}\text{-Li}_2\text{FeS}_2$ composites with CAM volume fractions between 0.32 and 0.74 and the active material itself have been determined by chronoamperometry. For characterization of the electronic conductivity, the samples are placed between stainless steel current collectors creating ion-blocking, electron-conducting conditions. Analogous, for characterization of the ionic conductivity, samples have been sandwiched between layers of $\text{Li}_{5.5}\text{PS}_{4.5}\text{Cl}_{1.5}$ and In/LiIn to create electron-blocking, ion-conducting conditions. Hereby, $\text{Li}_{5.5}\text{PS}_{4.5}\text{Cl}_{1.5}$ blocks the electronic transport while the In/LiIn acts as Li^+ reservoir to allow constant Li^+ current buildup.

Chronoamperometry experiments were conducted by applying a constant voltage varying between -45 mV and 50 mV or 1 mV and 8 mV, for the electronic and ionic transport characterization, respectively and measuring the current response. The applied voltages for the case of electronic transport and ionic transport are depicted as a function of experiment time in Figure S2 and Figure S3, respectively. The volume

fraction of CAM ϕ_{CAM} identifying the different composites is shown in the inset of the plots.

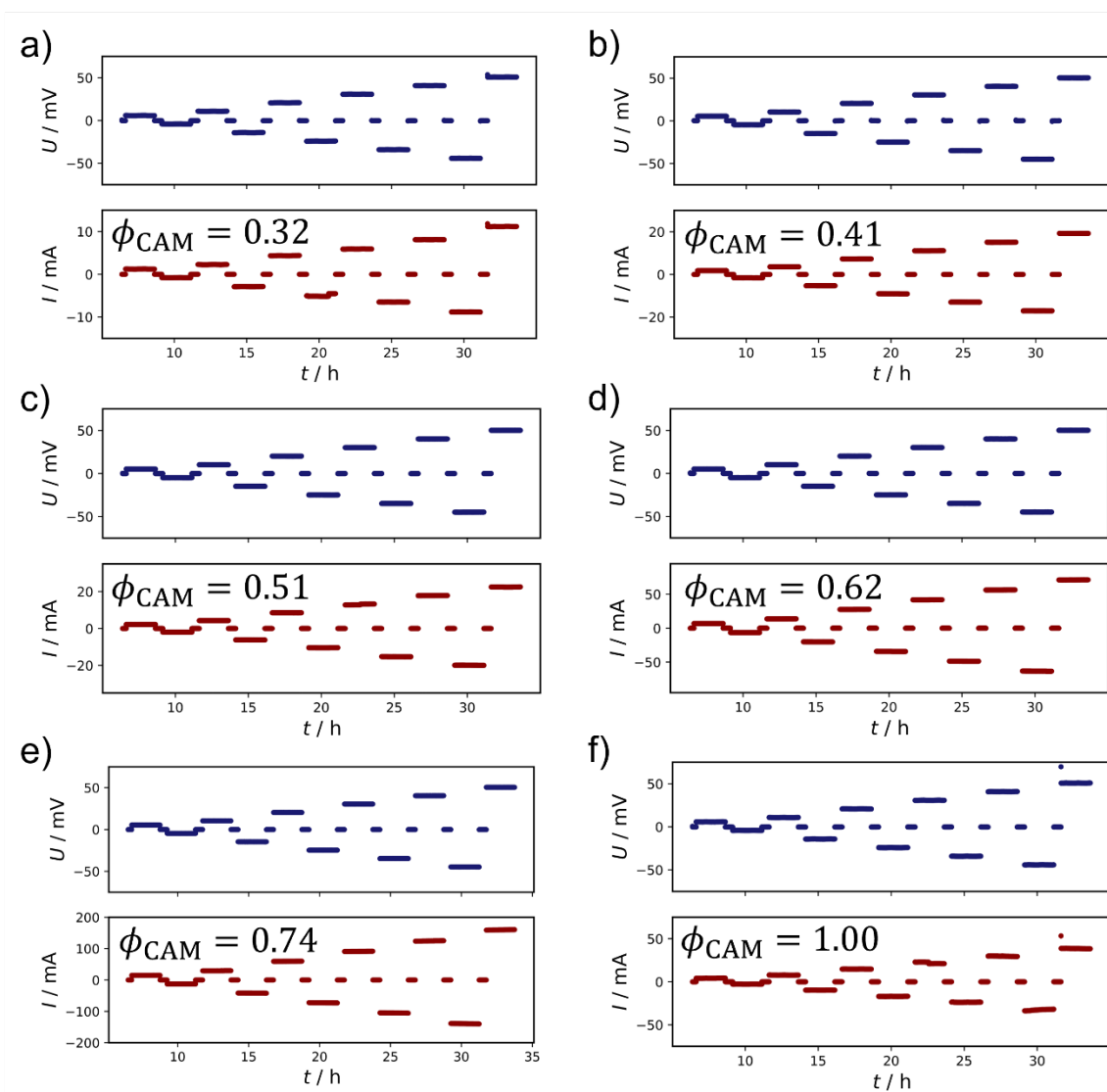


Figure S2. Applied voltage and current response of the system (electron conducting, ion blocking conditions) for cathode composites with volume fractions between 0.32 and 0.74 (shown in a) to e) in order of volume fraction increase) and f) Li_2FeS_2 .

For electronic transport, the voltage was applied for two hours to create a steady-state response, while for ionic transport, the equilibration time was extended to five hours.

This was necessary to reach steady-state conditions considering the significantly lower conductivity of ions as shown in main text Figure 4 a.

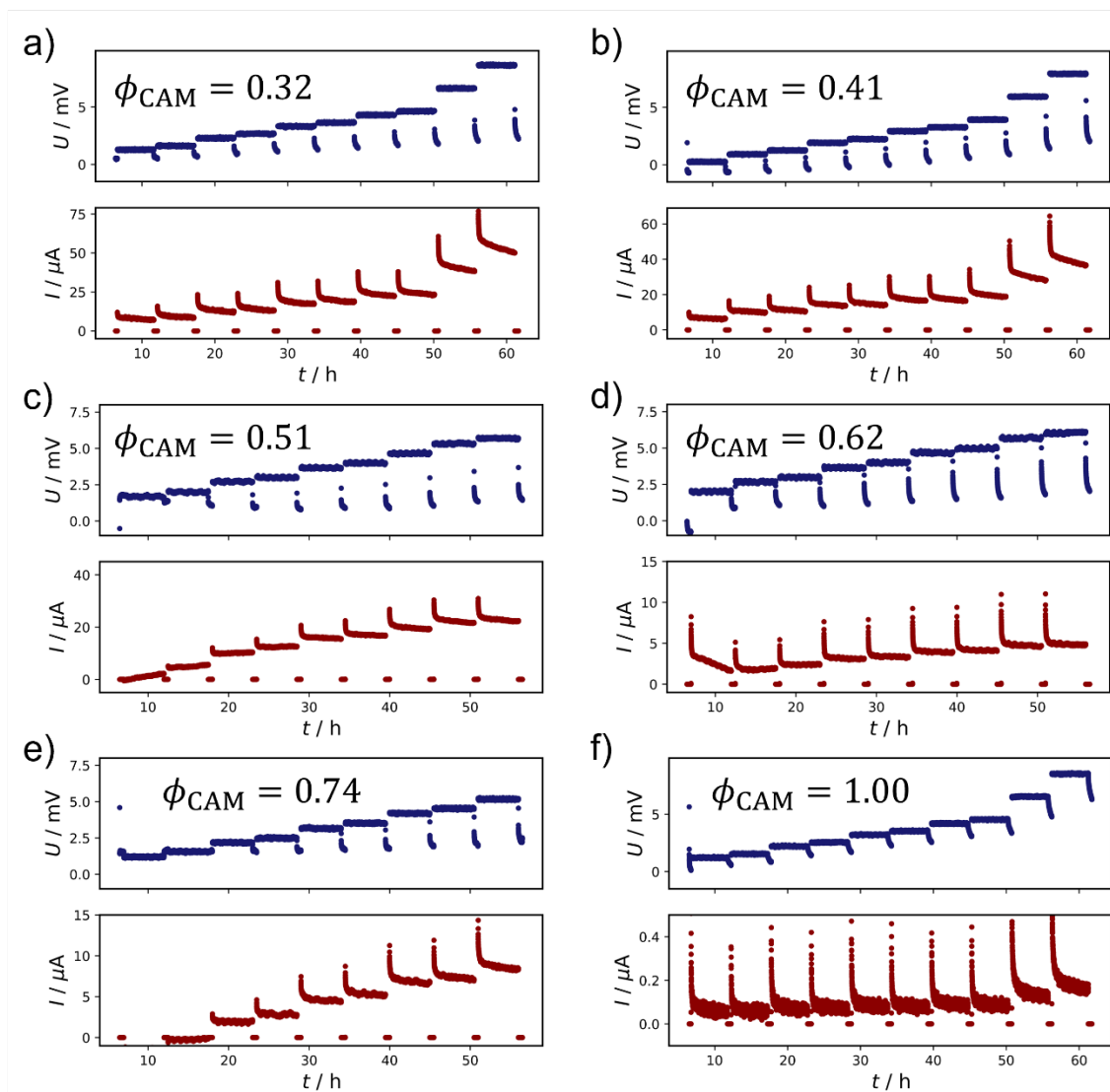


Figure S3. Applied voltage and current response of the system (electron blocking, ion conducting conditions) for cathode composites with volume fractions between 0.32 and 0.74 (shown in a) to e) in order of volume fraction increase) and f) Li_2FeS_2 .

The ionic and electronic resistance of the system are determined from the linear relation between applied voltage and resulting current, following Ohms law and $U =$

$R \cdot I$. The characteristic U - I curves and linear fits are depicted in Figure S4 and Figure S5 for determination of the electronic and ionic conductivity, respectively.

In the case of the ionic conductivity measurements, the resistance contributions from the $\text{Li}_{5.5}\text{PS}_{4.5}\text{Cl}_{1.5}$ layers are subtracted considering their thickness and the ionic conductivity of $\text{Li}_{5.5}\text{PS}_{4.5}\text{Cl}_{1.5}$. Finally, the conductivities are calculated from the resistance and the geometry of the sample (thickness h and area A), following:

$$\sigma_{\text{ion},e} = \frac{1}{R_{\text{ion},e}} \cdot \frac{h}{A} \quad \text{Eq. S1}$$

The uncertainty of σ_e considering the uncertainty of the linear fit are below 2% for all compositions. The respective uncertainty of σ_{ion} is in the range between 8% and 3% for all compositions. The relative densities as calculated from the mass and the measured geometrical sample parameters are $\approx 85\%$ for all investigated samples.

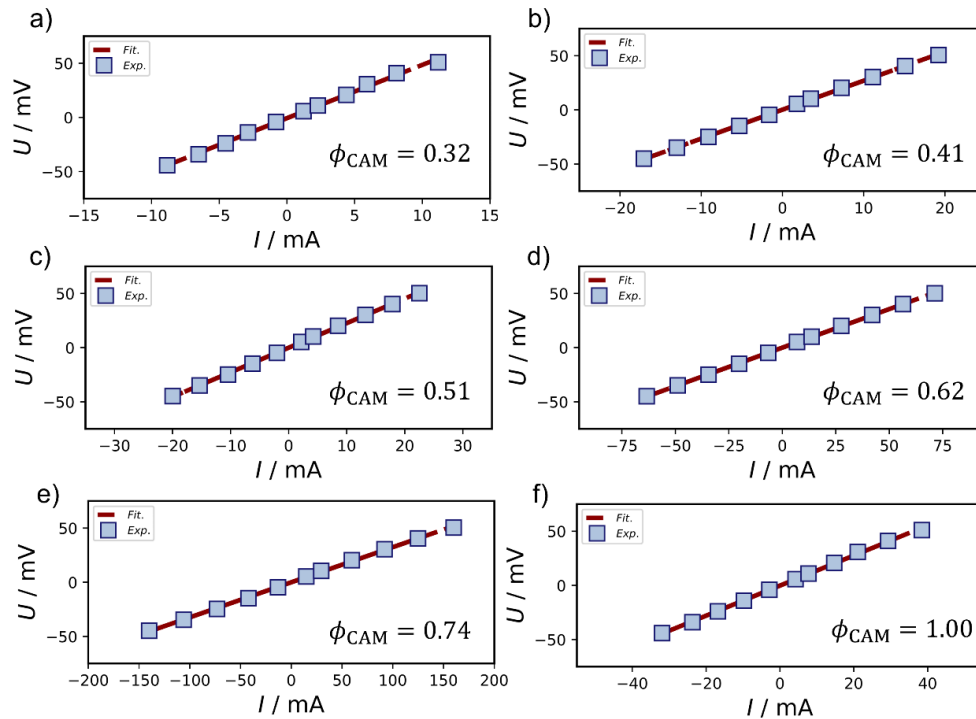


Figure S4. U - I curves and the linear fit to extract the electronic resistance of the system for a) to e) all investigated cathode compositions and f) Li_2FeS_2 .

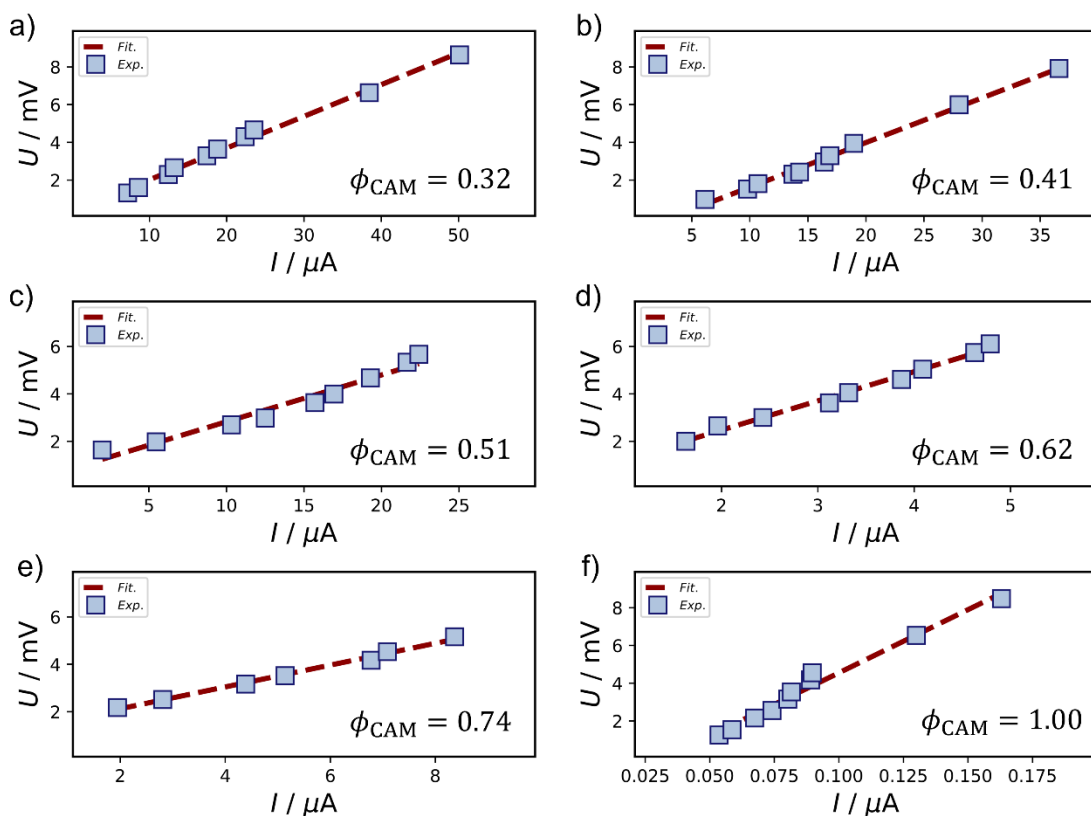


Figure S5. U - I curves and the linear fit to extract the ionic resistance of the system for a) to e) all investigated cathode compositions and f) Li_2FeS_2 .

Impedance spectroscopy and transmission line modelling

Impedance spectroscopy was measured in half-cell configuration of the as-assembled cells before conducting any electrochemical characterization. The experimental details are given in the methods section of the main text. The measured impedance spectra are evaluated with a Z-type transmission line model,² that describes electron-blocking conditions at the cathode-separator interface, and ion-blocking conditions at the cathode-current collector interface. All acquired impedance spectra, the corresponding fit to the data and the Z-type transmission line model are shown in Figure S6. The impedance contribution $Z_{\text{SE+In/LiIn}}$ describes contributions from the separator, described with a resistor, and of the separator In/LiIn interface, described with a resistor parallel to a constant-phase element. The transmission paths itself are made

of simple resistors to describe the ionic R_{ion} and electronic R_e resistance in the cathode, interconnected with a constant-phase element.

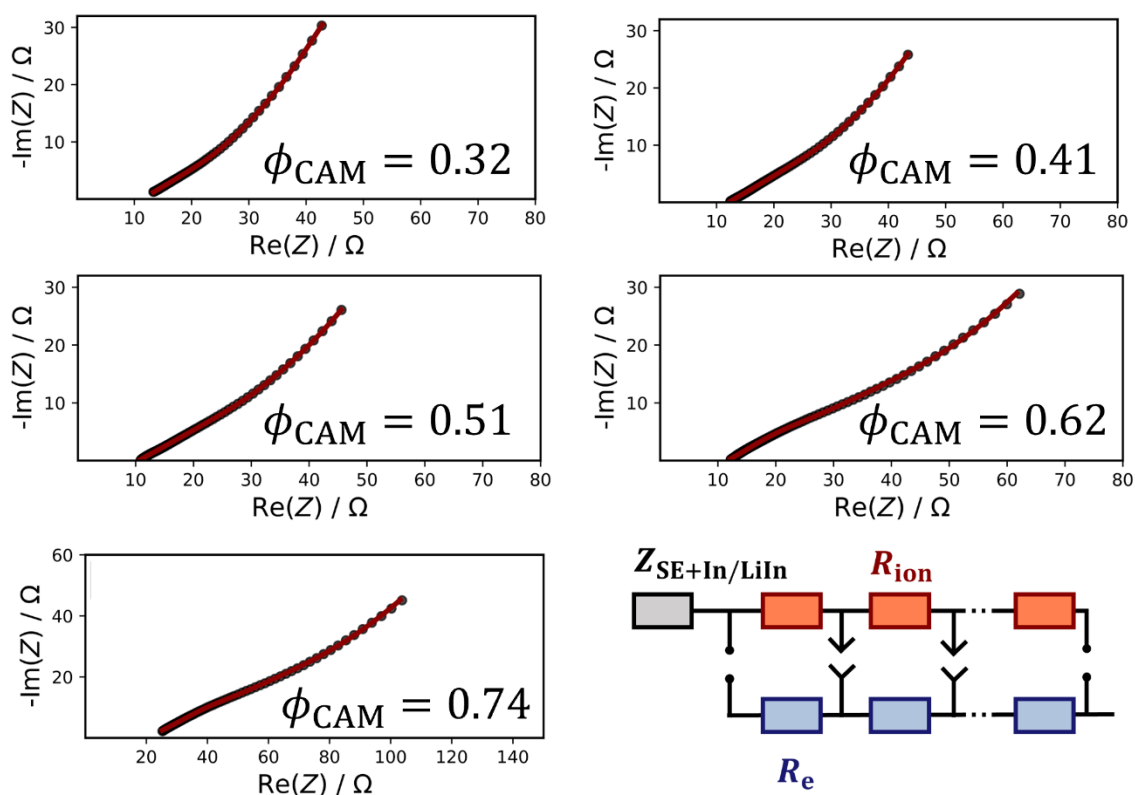


Figure S6. Impedance spectra and transmission-line model fit for all investigated cathode composite compositions (see legend) in half cells using $\text{Li}_{5.5}\text{PS}_{4.5}\text{Cl}_{1.5}$ as separator and Li/LiIn as reference electrode. The utilized transmission line model is depicted in the bottom right.

Initially, the expected resistance values of the separator, the ionic and electronic path of the cathode, were calculated from the respective conductivities and used to initialize the model. Following, $Z_{\text{SE+In/LiIn}}$, i.e., the resistance of the separator and impedance of the In/LiIn interface were fit while R_{ion} and R_e were fixed. Afterwards, R_{ion} was fit against the data while R_e was kept constant. This was done since R_e approaches zero considering the high electronic conductivity of the electrolytes, and large uncertainties followed fitting these low resistance contributions in the impedance

spectra. Finally, all fitting parameters were opened simultaneously, and the ionic conductivities of the cathode were calculated following Eq. S2. The resulting ionic conductivities agree with the results from the chronoamperometry experiments and a comparison is shown in Figure S6. The average and standard deviation of the comparison of both techniques is given in the main text (Figure 4 a).

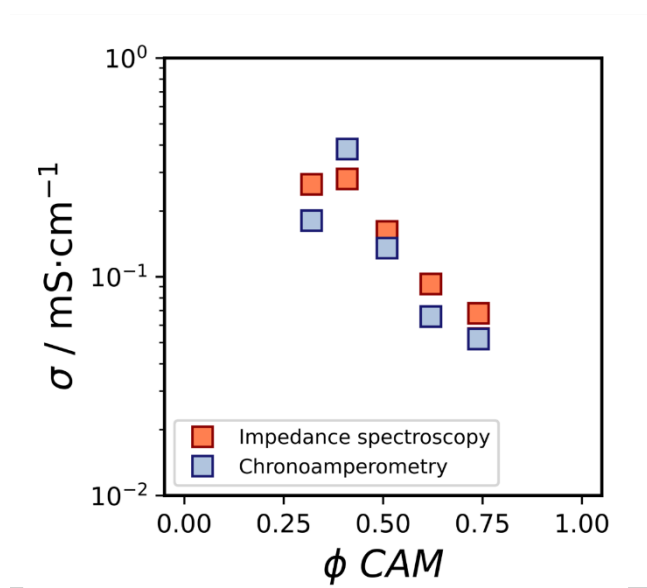


Figure S7. Comparison of the ionic conductivity obtained from chronoamperometry (blue) and impedance spectroscopy (red) experiments.

Effective medium modelling of the partial conductivities

In this work we have utilized an effective medium model derived by Wu and coworkers³ and the main equations are restated in the following. Nonetheless, many similar expressions and special case effective medium models exist and the reader is referred to the overview given by McLachlan, Blaszkiewicz and Newnham.⁴ The model takes the form of a general effective medium theory:

$$\frac{\sigma_{\text{eff}} - \sigma_1}{k \cdot \sigma_{\text{eff}} + \sigma_1} \phi_1 + \frac{\sigma_{\text{eff}} - \sigma_2}{k \cdot \sigma_{\text{eff}} + \sigma_2} \phi_2 = 0, \quad \text{Eq. S2}$$

where σ_{eff} is the effective conductivity of the composite and σ_1 , σ_2 , ϕ_1 and ϕ_2 are the conductivities and volume fractions of the composite constituents, respectively. In the derivation of the model, $k = \left(\frac{Z}{2} - 1\right)$ where Z is a measure for the connectivity of particles in a perfectly regular composite.³ Eq. S2 is a general equation in effective medium theory, while the interpretation of the constant k can vary between models.⁴⁻

6

The general formulation can be solved for the effective conductivity σ_{eff} under the condition that $\phi_1 + \phi_2 = 1$, leading to the expression used for fitting of the data in the main text:

$$\sigma_{\text{eff}} = \frac{E_1 + \sqrt{E_1^2 + E_2}}{2k} \quad \text{Eq. S3}$$

where E_1 and E_2 are defined as:

$$E_1 = (k + 1)(\sigma_1 \phi_1 + \sigma_2 \phi_2) - (\sigma_1 + \sigma_2) \quad \text{Eq. S4}$$

$$E_2 = 4k\sigma_1\sigma_2. \quad \text{Eq. S5}$$

Finally, Eq. S2 is used to fit the experimental ionic and electronic conductivities and the results are shown in main text Figure 4. During the fitting procedure, the conductivity of the lower conducting phase, CAM for ion and SE for electron transport, was kept to the expected experimental values, while the conductivity of the faster conducting phase and k was fit. Given that k is proposed to be a microstructural constant, it was constrained for both transport paths in first approximation. Moreover, logarithmic weighting was applied during the fitting procedure given the exponential change of both conductivities with the volume fraction of CAM. The resulting value of $k = 3.55 \pm 0.25$.

Electrode microstructure

Scanning electron micrographs (SEM) and energy dispersive X-ray spectroscopy (EDX) were utilized to characterize the microstructure of composites with different composition. No significant differences were observed throughout the series as shown by the representative micrographs, and Cl (to identify the SE) and Fe (to identify the CAM) EDX signals of composites with $\phi_{CAM} = 0.32, 0.51$ and 0.74 (Figure S8).

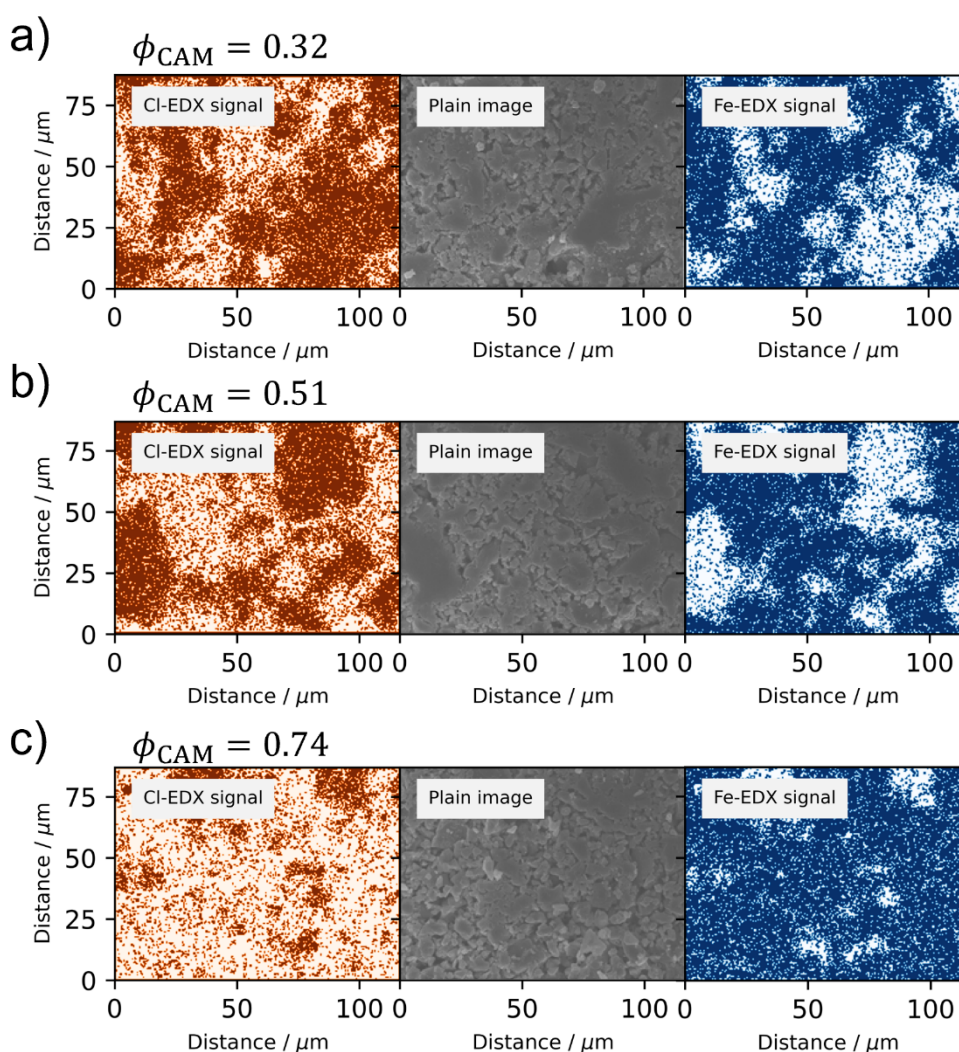


Figure S8. SEM and EDX investigation of composite pellets with a) $\phi_{CAM} = 0.32$, b) 0.51 and c) 0.74 . The Cl-EDX signal (identifying $Li_{5.5}PS_{4.5}Cl_{1.5}$) is shown on the left, the plain SEM image in the middle and the Fe-EDX signal (identifying Li_2FeS_2) on the right.

Voltage profiles

Exemplary voltage profiles for electrodes of all compositions (in thin electrode configuration) are given in Figure S9.

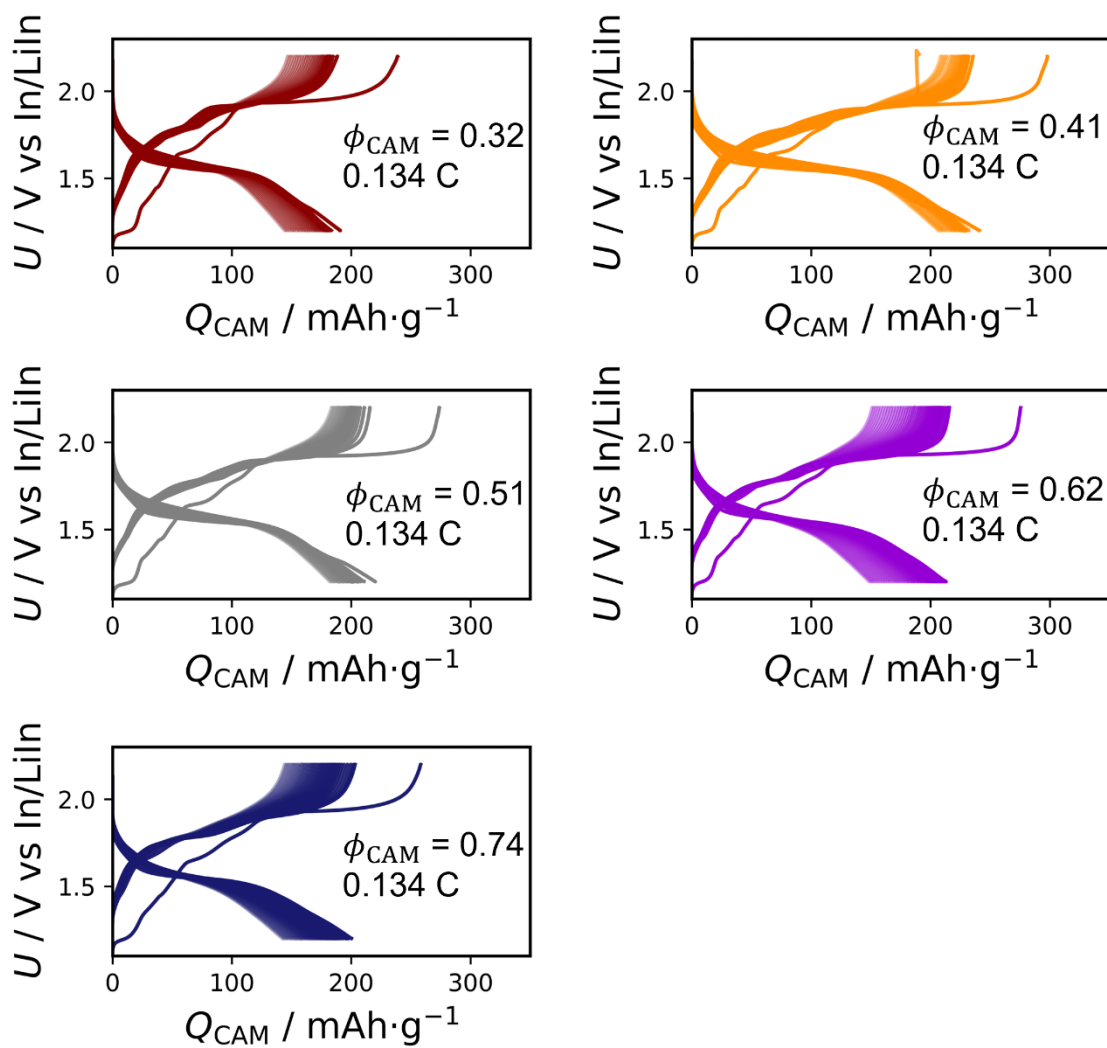


Figure S9. Voltage profiles obtained at 0.134 C for cells using cathode composites of varying composition. The volume fraction of CAM in the respective composite is given in the inset, labelling the datasets. The shown data are exemplarily for cells of that composition of which at minimum triplicates have been prepared.

Additionally, the derivative of the specific capacity with voltage, dQ/dV , was analyzed to gather more information about the voltage plateaus during cycling. No significant or systematic changes in the charge and discharge characteristics were observed within the series, with two plateaus during charging corresponding to oxidation of Fe^{2+} to Fe^{3+} (around 1.7 to 1.8 V), and the formal oxidation of S^{2-} to $(\text{S}_2)^{2-}$ (around 1.9 V) and one reduction peak around 1.5 to 1.6 V. Representative plots for all compositions are given in Figure S10.

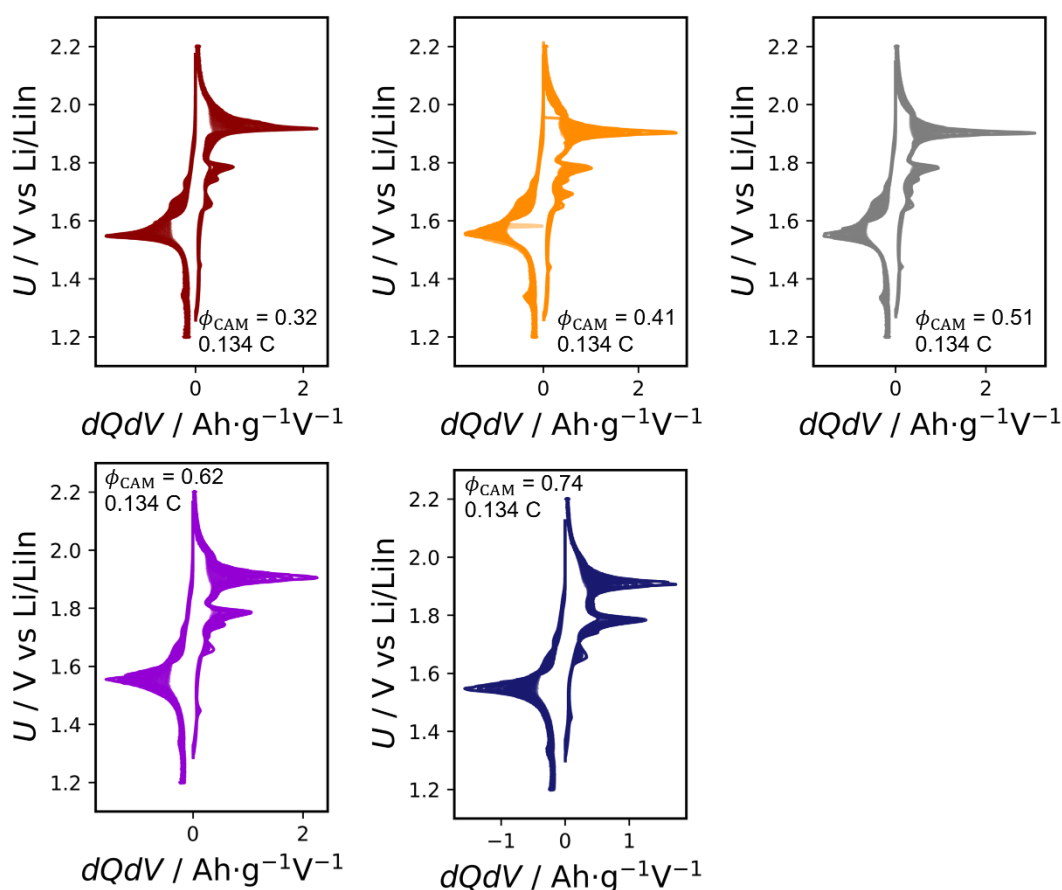


Figure S10. The derivative dQ/dV for cells with varying composite composition (indicated by label inside the subplots) as a function of cycling. The derivatives correspond to the voltage profiles shown in Figure S9.

Rate retention of cathodes with increased thickness

Rate retention for $\phi_{CAM} = 0.32, 0.51$ and 0.74 is shown in main text Figure 5 b. The additional rate retentions of cells with $\phi_{CAM} = 0.74$ and increased cathode thicknesses are shown in Figure S11.

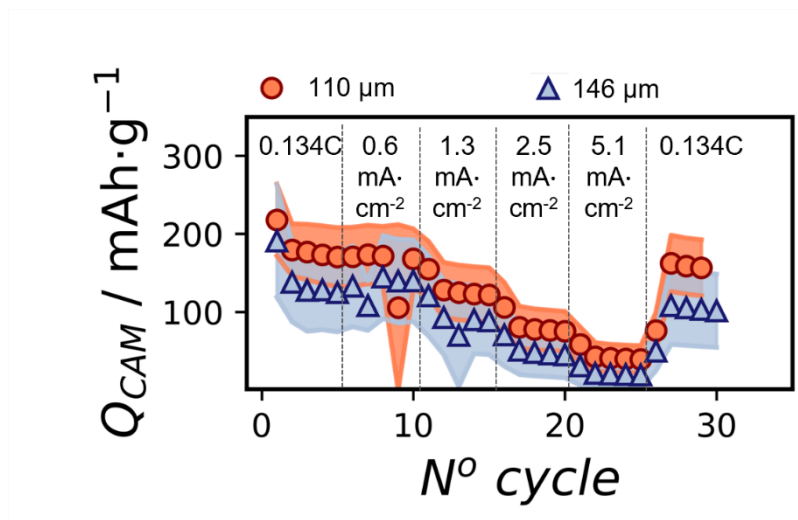


Figure 11. Rate retention of cathodes with $\phi_{CAM} = 0.74$ and increased thickness.

The capacity retention as a function of the applied current density is depicted in Figure S12 for all investigated cathodes.

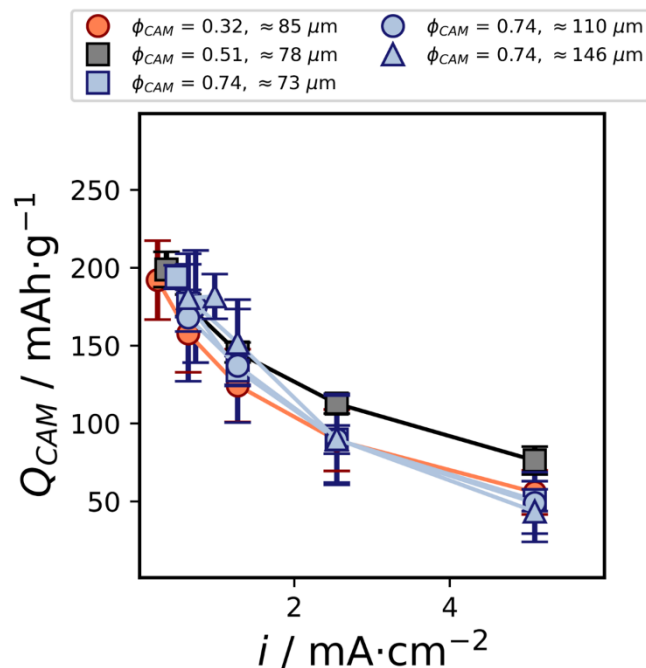


Figure S12. Rate retention of all investigated cathodes as a function of the applied current density.

Overview of the δ -parameter against the cathode utilizations

A multitude of cathodes with different δ values have been investigated. This is, because δ changes with composition because of the effective conductivity changes, the cathode thickness and the current density during rate testing. An overview about all δ values and the capacities achieved at these values is given in Figure S13. While quantitative trends can be observed, there is no overarching direct relation between δ and the cathode utilization measured by Q_{CAM} .

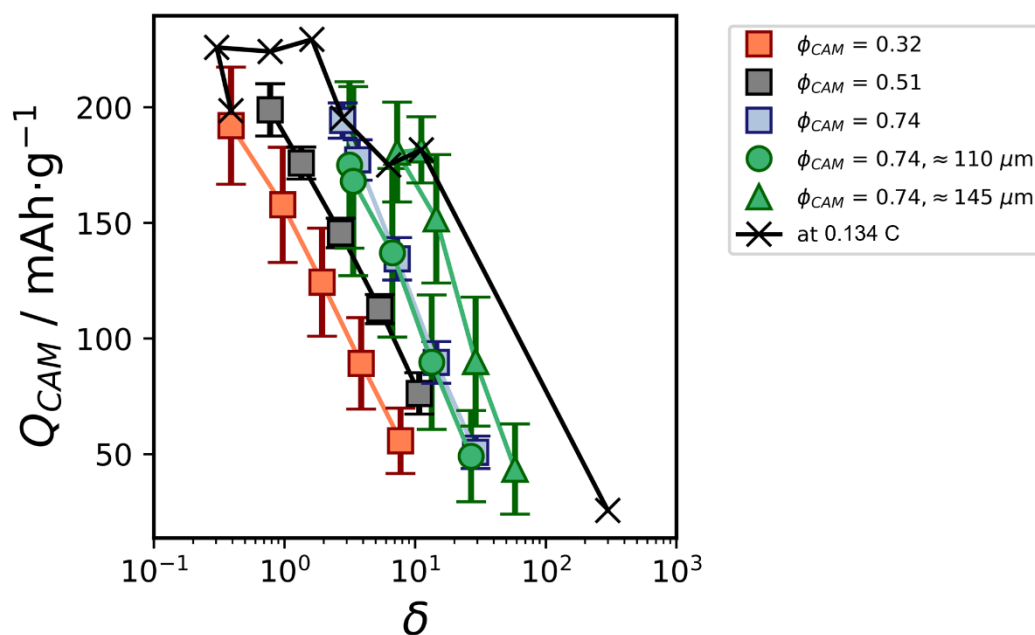


Figure S13. Comparison between the δ -parameter of cathodes containing in comparison to the achieved capacities (per mass active material, Q_{CAM}). The dataset “at 0.134 C” includes cells at various composition and thickness at the same C-rate and resembles the data plotted in Figure 6 a of the main text. All other datasets represent the current density dependence of Q_{CAM} and δ .

References

- 1 A. Gautam, M. Ghidui, E. Suard, M. A. Kraft and W. G. Zeier, *ACS Appl. Energy Mater.*, 2021, **4**, 7309–7315.
- 2 Z. Siroma, N. Fujiwara, S. I. Yamazaki, M. Asahi, T. Nagai and T. Ioroi, *Electrochim. Acta*, 2015, **160**, 313–322.
- 3 Z. Wu and M. Liu, *Solid State Ionics*, 1996, **93**, 65–84.
- 4 D. S. McLachlan, M. Blaszkiwicz and R. E. Newnham, *J. Am. Ceram. Soc.*, 1990, **73**, 2187–2203.
- 5 B. Tjaden, S. J. Cooper, D. J. Brett, D. Kramer and P. R. Shearing, *Curr. Opin.*

Chem. Eng., 2016, **12**, 44–51.

6 D. A. G. Bruggeman, *Ann. Phys.*, 1935, 24, 636-663